Atomic-Level Description of Thermal Fluctuations in Inorganic Lead Halide Perovskites

THE JOURNAL OF PHYSICAL CHEMISTRY LETTERS
A JOURNAL OF THE AMERICAN CHEMICAL SOCIETY

pubs.acs.org/JPCL

Letter

Atomic-Level Description of Thermal Fluctuations in Inorganic Lead Halide Perovskites

Oliviero Cannelli, Julia Wiktor, Nicola Colonna, Ludmila Leroy, Michele Puppin, Camila Bacellar, Ilia Sadykov, Franziska Krieg, Grigory Smolentsev, Maksym V. Kovalenko, Alfredo Pasquarello, Majed Chergui,* and Giulia F. Mancini*

Cite This: *J. Phys. Chem. Lett.* 2022, 13, 3382−3391

Read Online

ACCESS | Metrics & More | Article Recommendations | Supporting Information

ABSTRACT: A comprehensive microscopic description of thermally induced distortions in lead halide perovskites is crucial for their realistic applications, yet still unclear. Here, we quantify the effects of thermal activation in $CsPbBr_3$ nanocrystals across length scales with atomic-level precision, and we provide a framework for the description of phase transitions therein, beyond the simplistic picture of unit-cell symmetry increase upon heating. The temperature increase significantly enhances the short-range structural distortions of the lead halide framework as a consequence of the phonon anharmonicity, which causes the excess free energy surface to change as a function of temperature. As a result, phase transitions can be rationalized via the soft-mode model, which also describes displacive thermal phase transitions in oxide perovskites. Our findings allow to reconcile temperature-dependent modifications of physical properties, such as changes in the optical band gap, that are incompatible with the perovskite time- and space-average structures.

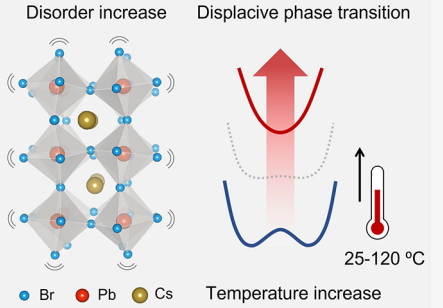

The implementation of lead halide perovskites as active medium in photovoltaic and optoelectronic devices is currently hindered by their relatively poor long-term stability.[1,2] Indeed, despite their promising performances,[3,4] these materials suffer from degradation under operative conditions, caused by external factors such as oxygen, moisture, and light.[5−7] Composition and structural instabilities were also observed, due to ion migration,[8] phase segregation,[9] and thermal heat effects.[10] Even though effective strategies to mitigate some of these issues are already under development, as in the case of degradation due to moisture,[11,12] solutions to other forms of instabilities still require additional investigation. Specifically, thermal and optical stimuli, which represent two forms of functional activation respectively exploited for thermoelectrics[13−15] and optoelectronics,[16,17] are also possible sources of degradation.

The perovskite structural instabilities are closely related to the peculiar flexibility of the Pb−X ($X = Cl^-$, Br^-, I^-) lead halide framework, characterized by pronounced lability and phonon anharmonicity.[18−24] The deformable lattice results in small free energy formation of anion vacancies and low activation energy for vacancy-mediated transport, implying intrinsic high anion mobility[25] and causing reversible phase separation when multihalide perovskites are exposed to continuous illumination.[9]

The study of a photoexcited system requires to disentangle optically induced electronic effects from possible thermal ones. In a recent work on $CsPbBr_3$ nanocrystals (NCs),[26] we demonstrated that thermal effects are not significant in the photoinduced response, which is characterized by polaronic lattice distortions that we specifically quantified with atomic-level precision. Here, we focus on the characterization of the temperature (T)-induced response of the $CsPbBr_3$ NCs in a temperature range relevant for optoelectronic applications. We therefore provide a comprehensive description of $CsPbBr_3$ perovskite nanocrystals dynamics, and we clarify that lattice flexibility is underpinning fundamentally different responses upon photo- *or* thermal activation.

The structure of $CsPbBr_3$ consists of a Pb−Br inorganic sublattice in which the Pb^{2+} ions are surrounded by 6 Br^- anions, making a framework of corner-sharing octahedra. The cuboctahedral voids left in the crystal are filled by the Cs^+ ions, creating a complementary sublattice where the cations undergo a free rattling motion.[19] In single crystals, the phase diagram of this system was determined by neutron and X-ray diffraction (XRD) studies, which identifies phases of increasing symmetry upon temperature rise: orthorhombic *Pnma* (T < 88 °C),

Received: January 28, 2022
Accepted: March 25, 2022
Published: April 11, 2022

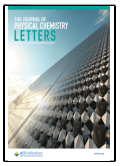

https://doi.org/10.1021/acs.jpclett.2c00281
J. Phys. Chem. Lett. 2022, 13, 3382−3391

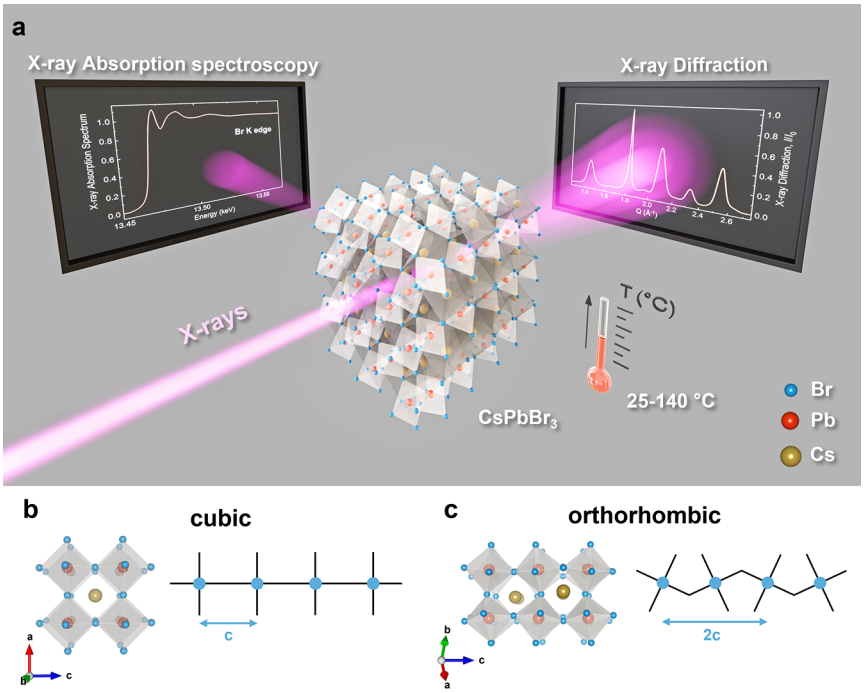

Figure 1. (a) Multiscale probing of thermally induced changes in $CsPbBr_3$ perovskite nanocrystals: schematic layout of the experiment. T-dependent XRD and XANES measurements were conducted in parallel on $CsPbBr_3$ dry nanocrystals, respectively at 12.9 keV and at the Br K-edge (13.450−13.570 keV). Courtesy of Balázs Őrley. $CsPbBr_3$ crystal structures: (b) $Pm\bar{3}m$ cubic and (c) *Pnma* orthorhombic unit cell graphics, each with a schematic for the tilting of the inorganic framework. In the orthorhombic phase, the ordered tilting of the $PbBr_6$ octahedra causes the doubling of the unit cell constant along the crystallographic *c*-axis.[50]

tetragonal $P4/mbm$ (88 °C < T < 130 °C), and cubic $Pm\bar{3}m$ (T > 130 °C).[27,28] In recent years, this simple description in terms of transformations of ideal lattices across the phase diagram was questioned, even though the presence of structural disorder at high temperatures was already suggested in the seminal work of Møller on inorganic lead halide perovskites single crystals.[29] Thermal distortions of the cubic unit cells were shown in both methylammonium (MA^+) and cesium lead bromide single crystals through first-principles molecular dynamics (MD) and low-frequency Raman scattering.[22] T-induced rotational disorder of lead halide octahedra was also observed in a high energy resolution inelastic X-ray scattering (HERIX) and pair distribution function (PDF) study on $MAPbI_3$ single crystals at 350 K, ascribing the effect to the phonon anharmonicity of the Pb−I cage.[20]

In nanostructured perovskites, the scenario is even more complex, as many physical properties are influenced by the dimensionality of the structure. XRD measurements on $CsPbBr_3$ perovskite NCs showed the impact of the system's size on the phase diagram, with phase transitions observed at lower temperatures with respect to their bulk counterpart, in the ranges T = 50−59 °C and T = 108−117 °C, ascribed to the unit cell changes orthorhombic-tetragonal and tetragonal-cubic, respectively.[21] Conversely, approaches beyond standard Rietveld refinement methods highlighted the structural defectiveness of inorganic lead halide NCs. This was associated with orthorhombic twinned subdomains both at room and higher temperatures,[23] suggesting that multiple structural configurations are copresent in the system. The dimensionality of the NCs also affects the thermal transport, which changes from the diffusive regime to the ballistic limit when the size of the structure is smaller than the inelastic phonons mean-free path of the semiconductor,[30] and it is routinely exploited to tune the band gap and photoluminescence spectra of lead halide perovskites. Furthermore, ligand-capping strategies, which are often employed to enhance the NC system's stability,[12,31] also modify the charge carriers relaxation[32] and opto-mechanical properties of these structures.[33] As a result, a direct comparison between bulk and NCs is often misleading.

Even though a large variety of experimental and computational methods have been employed to investigate the flexibility of the lead halide structure, a unified picture simultaneously describing T-induced changes in the short-range and in the long-range is still missing. Additionally, the reported static and dynamic local disorder is in contrast with the assignment of highly ordered phases in the long-range, especially at high temperatures, raising questions about the phase diagrams proposed in early works[27,28,34] and its validity to describe key properties of the system. Some studies ascribed the perovskites high-temperature phase to an apparent cubic structure resulting from the statistical average of disordered local structures,[20,22,23] but the disorder itself was never fully reconciled with the presence of well-defined phase transition temperatures. Conversely, Monte Carlo simulations at finite-temperatures assigned the qualitative features of the phase transitions of $CsPbBr_3$ to pure thermal lattice activation;[35] however, the authors did not benchmark their theoretical results against experimental observables.

Here, we present a correlative characterization of the short-range and long-range structures in T-activated $CsPbBr_3$ NCs. We performed T-dependent measurements of Br K-edge X-ray absorption near edge structure (XANES) spectroscopy and powder XRD on $CsPbBr_3$ NCs in the 25−140 °C range, i.e., across the phase diagram of the nanostructured material, and compare them to *ab initio* MD calculations as a function of temperature. The XANES and XRD observables were

https://doi.org/10.1021/acs.jpclett.2c00281
J. Phys. Chem. Lett. 2022, 13, 3382−3391

computed as averages over several configurations extracted from the MD trajectory, with the XANES spectra additionally including core hole final state effects. This approach goes beyond standard structural refinement methods and fully accounts for the statistical fluctuations of the lattice structure.

The XANES shows that T-dependent short-range changes *cannot* be accurately described by average lattice structures from PDF refinement. Instead, the system dynamically adopts multiple local configurations that are characterized by pronounced structural deformations with respect to the ideal symmetries. In the high temperature phase, these lattice distortions have a magnitude comparable to those of the low-symmetry orthorhombic phase, but the stronger thermal fluctuations cause the long-range periodicity of the lattice to break, reproducing the T-dependent changes of the XRD experiment. Our observations are ascribed to the intrinsic phonon anharmonicity of the lead halide sublattice and are rationalized in terms of displacive thermal phase transitions via the soft-mode model.[36] This conceptual framework provides a thorough description of the physical properties of the system upon thermal heating, as in the case of band gap increase,[37] which cannot be captured by scenarios that preserve high symmetry lattice structures at the local scale.

Moreover, these results highlight the difference between thermal and light-induced structural responses in $CsPbBr_3$ perovskites, the former being intrinsically random in nature and the latter selectively driven by electron−phonon coupling.[26] The deeper understanding of the perovskite responses upon different stimuli will open new opportunities for manipulating and stabilizing the lattice structure in realistic applications.

T-dependent XANES and XRD measurements were performed at the SuperXAS beamline at the Swiss Light Source (SLS) of the Paul Scherrer Institute. The concept of the experiment is depicted in Figure 1a. The sample consists of a powder of long-chain zwitterion-capped $CsPbBr_3$ dry perovskite NCs with cuboidal shape (side length 11.9 ± 2.2 nm) and high photoluminescence quantum yield.[31] The sample was located in a thermostated cell holder between two 0.254 mm-thick graphite layers, and the internal temperature of the cell was calibrated and monitored throughout the experiment with a thermocouple.

T-dependent XRD measurements were performed using a monochromatic 12.9 keV X-ray beam in transmission geometry, with a sample−detector distance of 24.1 cm. The transmitted diffraction signal was acquired using a Pilatus 100k 2D detector (94965 pixels, 172 × 172 μm^2 pixel area) and then azimuthally averaged in the 1.3−2.8 $Å^{-1}$ Q-range to obtain the radial averaged intensity $I(Q)$

$$I(Q) = \frac{1}{2\pi}\int I(Q, \varphi)d\varphi$$

where $I(Q, \varphi)$ represents the scattered intensity at the defined scattering vector Q and azimuthal angle φ. The background XRD signal generated by the graphite sheets was isolated in a dedicated measurement, without the perovskite sample. In-depth information on XRD data analysis is available in the Supporting Information (SI). T-dependent XANES measurements were conducted using a 5-element silicon drift detector (SDD) for fluorescence detection at 90° geometry. The spectra were collected at the Br K-edge (13.450−13.569 keV) using a crystal silicon (111) monochromator. At each energy point, the spectra were normalized by the incident X-ray flux. A flat pre-edge offset was subtracted for each spectrum, and the intensity was normalized by the absorption edge integral. XRD patterns and XANES spectra were recorded in the 25−140 °C temperature range, exploring the entire phase diagram of the nanocrystalline system. $CsPbBr_3$ lattice structures for the *ideal* cubic and orthorhombic unit cells are depicted in Figure 1b,c, respectively. With respect to the cubic symmetry, the orthorhombic phase is characterized by tilted $PbBr_6$ octahedra along both the equatorial and axial planes, with a deviation of the Pb−Br−Pb angle from the 180° value of the cubic unit cell. Model XRD $I(Q)$ profiles for orthorhombic and cubic unit cells are shown in Figure S2c, respectively bottom and top, as predicted in the VESTA software[38] at 12.9 keV X-ray incident energy.

Ab initio MD simulations based on density functional theory (DFT) were performed using the CP2K package.[39] The Perdew−Burke−Ernzerhof (PBE) functional[40] was used to describe the exchange-correlation energy. Three different MD simulations, lasting for 10−16 ps and using a time step of 5 fs, were carried out in the isobaric (NpT) ensemble. In the runs, the initial shape of the cell was kept constant, while the volume of the cell was allowed to fluctuate. One MD calculation was run at 27 °C (300 K) with the orthorhombic geometry as initial condition. At 130 °C (403 K), two simulations were run, one initialized with the cubic and one with the orthorhombic geometry. These structures were chosen to monitor the thermal dynamics of the system in its lowest and highest structural phases. For the high-temperature simulations, the two different starting geometries were considered in order to evaluate the impact of the initial conditions on the computation. Simulations were carried out in supercells containing 1080 atoms, which corresponds to the 6 × 6 × 6 repetition of the unitary cubic cell. The Brillouin zone was sampled solely at the Γ point. The first 5 ps of the simulations were considered as equilibration and excluded from the statistics. The mean XRD $I(Q)$ profiles were calculated averaging the scattering intensities predicted by VESTA[38] for instantaneous structures separated by 0.75 ps extracted from the MD trajectories. Three additional MD simulations, with the same parameters and starting conditions, were also performed for smaller supercells (320 atoms, corresponding to the 4 × 4 × 4 repetition of the unitary cubic cell) to generate structures for the computationally demanding XANES simulations.

XANES spectra were computed performing first-principles DFT calculations using the Quantum Espresso distribution.[41,42] The exchange-correlation effects were described using the PBE functional,[40] and the ultrasoft pseudopotentials from the PS-library[43] were employed to model the electron−ion interaction. Br K-edge spectra were simulated with the XSpectra code[44,45] within the excited-electron plus core-hole (XCH) approximation.[46] Calculations were based on 320-atoms structures obtained from *ab initio* MD simulations in the CP2K package,[39] corresponding to the 4 × 4 × 4 repetition of the unitary cubic cell. MD calculations were run at 27 °C (300 K) for an initial orthorhombic geometry and at 130 °C (403 K) for initial orthorhombic and cubic geometries. For each MD simulation, 5 structures corresponding to 5 different time delays of the MD trajectory were considered. For each time delay, 10 separate XCH calculations were performed with a core hole placed on a randomly chosen Br site of the supercell, for which the Br K-edge spectrum was computed. The final Br K-edge spectra result from the average of 10 Br sites in each of

https://doi.org/10.1021/acs.jpclett.2c00281
J. Phys. Chem. Lett. 2022, 13, 3382−3391

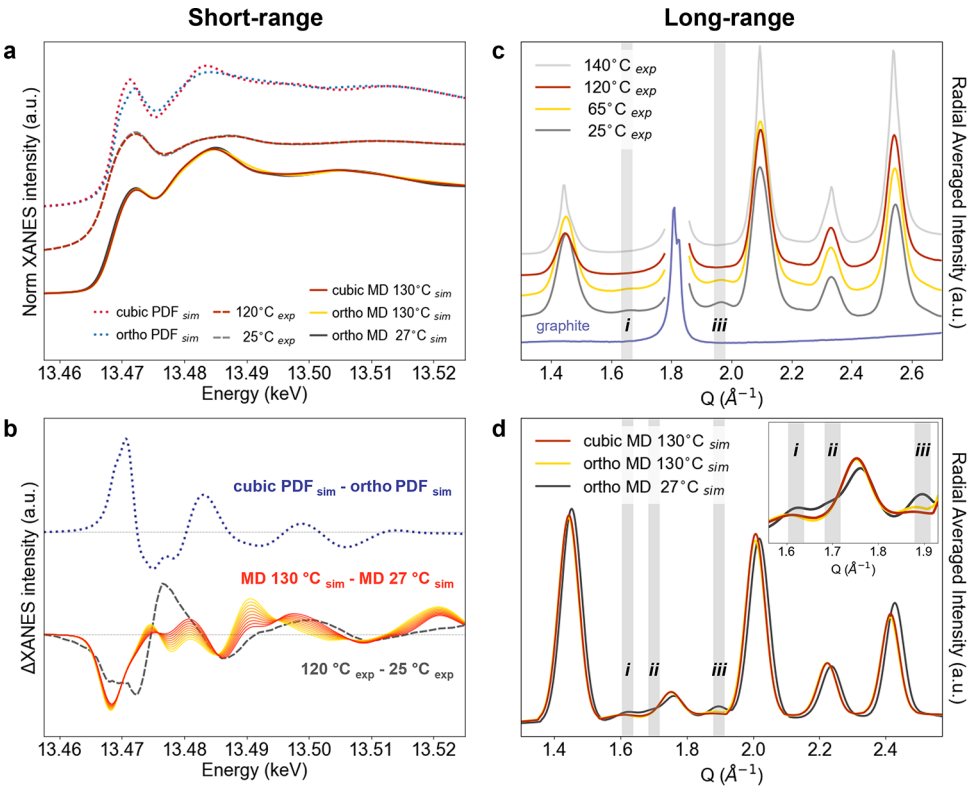

Figure 2. Correlative short- and long-range T-dependent structural characterization of $CsPbBr_3$. (a) Experimental Br K-edge XANES spectra of $CsPbBr_3$ NCs at 25 °C (dashed gray) and at 120 °C (dashed red), *ab initio* XANES spectra for the pristine orthorhombic and cubic structures obtained from a PDF refinement of XRD data[21] (dotted blue and dotted red, respectively), and *ab initio* XANES spectra for the MD simulations at 27 °C (orthorhombic starting symmetry, gray) and 130 °C (orthorhombic and cubic starting symmetries, yellow and red, respectively). All spectra were scaled by their underlying areas and vertically offset. (b) Br K-edge XANES differences for 120 °C minus 25 °C (experiment, dashed gray), pristine cubic minus pristine orthorhombic from PDF refinements (dotted blue) and the difference between the linear combinations of cubic 130 °C and orthorhombic 130 °C minus orthorhombic 27 °C MD simulations. The curves were obtained considering different coefficients of the cubic 130 °C and orthorhombic 130 °C MD spectra, from 100% cubic (red) to 100% orthorhombic (yellow). A 3-point adjacent averaging of the energy axis was performed for the experimental thermal difference, whereas the simulated spectral differences were multiplied by a factor ×0.30 (MD) and ×0.15 (pristine), the latter also being vertically shifted, to enable a straightforward comparison with the experiment. (c) Experimental XRD *I(Q)* profiles of $CsPbBr_3$ NCs as a function of the temperature from 25 to 140 °C. The sharp feature at 1.827 $Å^{-1}$ originates from the graphite peak enclosing the sample (blue curve). The shaded gray areas mark the region of the *(i)* and *(iii)* superlattice peaks, which disappear upon temperature increase. (d) XRD *I(Q)* profiles predicted from the MD simulations at 27 °C with orthorhombic starting geometry (gray), 130 °C with orthorhombic starting geometry (yellow) and 130 °C with cubic starting geometry (red). The shaded gray areas highlight the *(i)*, *(ii)*, *and (iii)* superlattice peaks. Inset: zoom into the 1.55−1.94 $Å^{-1}$ region of the superlattice peaks. In the legend of each panel, "ortho" stands for "orthorhombic".

the 5 MD structures, for a total of 50 spectra per MD simulation. Additional XCH simulations were performed for 160-atoms supercells which, were built starting from either the ideal orthorhombic or cubic unit cells, using the atomic coordinates reported in the literature from PDF refinements at 22 and 160 °C, respectively.[21] For each nonequivalent Br site, separate XCH calculations were performed, and the average Br K-edge XANES spectrum was computed. Details about the experimental and computational methods are described in the SI.

Figure 2 shows XAS and XRD results (experimental - top, and theoretical - bottom) obtained for the $CsPbBr_3$ system as a function of temperature. The Br K-edge experimental spectra (Figure 2a) collected for the NCs at 25 °C (dashed gray) and 120 °C (dashed red) show that the XANES spectrum is affected by the temperature increase both at pre-edge energies[47] and above the edge, which represents the ionization limit. Above the edge, the XANES spectrum is caused by single and multiple scattering events of the photoelectron emitted by the Br atoms against the neighboring atoms, and it contains information about bond angles and bond distances between the probed site and its nearest-neighbors.[48,49] The XANES traces were scaled by their total areas, and they exhibit a first peak at the Br edge (the so-called white line, at 13.472 keV), related to the Br 1s-4p electronic transition, followed by post-edge modulations peaked at 13.4875 and 13.510 keV. The temperature rise from 25 to 120 °C induces an intensity decrease of the main peaks and an intensity increase of the local minima, with an overall broadening of the spectral features. This is best visualized in Figure 2b where the difference between the 120 °C and the 25 °C experimental XANES spectra is reported in dashed gray. The data show a broad negative feature in the rising-edge region at energies 13.466−13.478 keV, with a global minimum at the edge position of 13.472 keV. A pronounced modulation is also observed up to 50 eV above the edge, with damped positive and negative features respectively peaked in the local minima and maxima of the steady-state spectra.

Figure 2a also shows the XANES spectra computed with *ab initio* simulation for MD calculations at 27 °C for an

https://doi.org/10.1021/acs.jpclett.2c00281
J. Phys. Chem. Lett. 2022, 13, 3382−3391

orthorhombic starting geometry (full gray curve) and at 130 °C for orthorhombic and cubic initial configurations (respectively, full yellow and full red curves). Although the two initial symmetries for the MD simulations at 130 °C are different, at this temperature the thermal activation lifts the original symmetry of the structure and dynamically distorts the lattice. This is consistent with the statistical evolution of the Pb−Br−Pb angle tilting over time (Figure S10) and the displacements of Cs, Pb, and Br sites with respect to their average positions (Figure S12), which show that the $CsPbBr_3$ lattice is characterized by pronounced local distortions and becomes dynamically more active with temperature. The minor differences in the predictions of the two calculations can be ascribed to the different boundary conditions imposed to the supercell for the two starting symmetries. We additionally show computations for the two pristine orthorhombic and cubic lattice structures (respectively, dotted blue and dotted red) as obtained from a PDF analysis of T-dependent XRD data reported in the literature.[21]

In all simulations, core hole final state effects were included, thus the difference between the XANES spectra of the MD and pristine structures lies on the presence or absence of local thermal fluctuations in the lattice. Specifically, the predictions of the MD simulations correspond to the *statistical average* of multiple XANES spectra of Br sites in different local environments. Instead, the calculations for the pristine structures reflect the XANES spectrum of a single time- and space-averaged configuration that preserves the translational symmetry in the long- and short-range, respectively orthorhombic (room temperature) or cubic (high temperature).

All simulations reproduce the Br K-edge main features; intensity deviations with respect to the experiment are due to systematic errors of the calculations which, however, cancel out when performing spectral differences between computed XANES spectra (Figure 2b). The two MD-simulated XANES traces at 130 °C have similar line shapes, both showing a blue shift of the rising edge and an intensity reduction of the main peaks at the energies 13.472 keV, 13.486, and 13.506 keV with respect to the MD simulation at 27 °C. A corresponding increase of the XANES intensity occurs at the energy of the local minima, in agreement with the experiment. Conversely, the comparison of the XANES spectra for the pristine cubic and orthorhombic structures shows that the former is significantly sharper than the latter and is characterized by one additional feature at 13.498 keV, in net contrast with the experiment.

The XANES differences for the orthorhombic and cubic MD simulations at 130 °C minus the orthorhombic MD simulation at 27 °C are shown in Figure 2b in yellow and red, respectively. In the same figure, we also present the curves obtained subtracting the orthorhombic MD simulations at 27 °C from different linear combinations of the XANES spectra for the orthorhombic and cubic MD simulations at 130 °C (color-coded from yellow to red upon an increasing relative weight of the cubic MD contribution). All linear combinations yield a negative dip centered at 13.468 keV, followed by a rise around 13.480 keV and intensity modulations at higher energies. The qualitative agreement with the experiment is very satisfactory, especially the post-edge modulations starting from 13.485 keV, despite the intensity mismatch of the feature at 13.477 keV. Instead, the spectral difference of the pristine cubic minus orthorhombic XANES spectra (dotted blue) consists in two positive peaks at 13.470 and 13.483 keV and a negative band between 13.4725 and 13.480 keV, followed by smaller post-edge modulations at higher energies. The first three features of this spectrum are completely absent in the experimental difference reported in Figure 2b and are traced back to the structural changes occurring when the translational symmetry of the lattice is artificially preserved on the local scale.

Overall, the short-range XANES characterization demonstrates an increment of the sublattice disorder caused by thermal fluctuations, leading to an overall broadening of the main spectral features with temperature. This finding points to the occurrence of a symmetry reduction in the local structure of the system, in contrast with the alternative picture of thermally induced symmetry increase suggested by previous long-range characterizations.[27,28] The scenario identified with the XANES directly reflects in the XRD results presented in the following.

The T-dependent XRD $I(Q)$ profiles measured in $CsPbBr_3$ NCs are shown in Figure 2c. The features highlighted by the gray shaded areas correspond to superlattice peaks that arise from the periodic recurrence of cooperative octahedral tilting in the orthorhombic lattice, which doubles the unit cell constant of the ideal cubic structure along the axis perpendicular to the tilting direction,[50] as represented in Figure 1b,c. The model $I(Q)$ profiles reported in Figure S2c show that the ideal orthorhombic unit cell is characterized by three superlattice peaks, labeled as *(i)*, *(ii)*, and *(iii)*; however, in our experiment, the pronounced peak at the 1.827 $Å^{-1}$ scattering vector, which comes from the background signal of the graphite sheets enclosing the sample, is superimposed to the superlattice peak *(ii)* and to the main reflections (022)-(202). In the range 25−120 °C, the main diffraction peaks preserve their shape and positions, whereas at 140 °C, the peak shapes change into a super-Lorentzian profile (see SI for further details). This effect points to incipient structural inhomogeneities of the sample occurring above the highest phase transition temperature, meaning that at lower temperatures the structural integrity of our sample is preserved. The disappearance of the superlattice peaks upon temperature increase up to 120 °C points to the loss of the octahedral tilting periodicity, an indication that, at this temperature, the system is in the highest temperature phase.

The XRD $I(Q)$ profiles predicted by *ab initio* MD simulations are reported in Figure 2d for three different starting conditions: 27 °C and orthorhombic symmetry (gray); 130 °C and orthorhombic symmetry (yellow); 130 °C and cubic symmetry (red). The MD simulation at 27 °C confirms the presence of the three superlattice peaks *(i)*, *(ii)*, and *(iii)* and indicates that, within the lattice thermal motion, the $PbBr_6$ octahedral tilting from which these features originate is preserved in the long-range, consistently with the orthorhombic room-temperature description of Figure 1c. Instead, the MD simulations at 130 °C lead to a strong decrease of the superlattice peaks intensity, correctly reproducing the high temperature XRD $I(Q)$ profile of our experiment.

Even though the disappearance of the *(i)*, *(ii)*, and *(iii)* superlattice peaks was generally ascribed to an order increase of the $CsPbBr_3$ unit cell from orthorhombic up to the cubic symmetry,[27,28] our results show that it is indeed occurring in the presence of sufficient thermal fluctuations. This effect causes the breaking of the long-range periodicity associated with the tilting of the room temperature orthorhombic structure depicted in Figure 1c, leading to a radically different conclusion from the lattice symmetry increase of Figure 1b.

https://doi.org/10.1021/acs.jpclett.2c00281
J. Phys. Chem. Lett. 2022, 13, 3382−3391

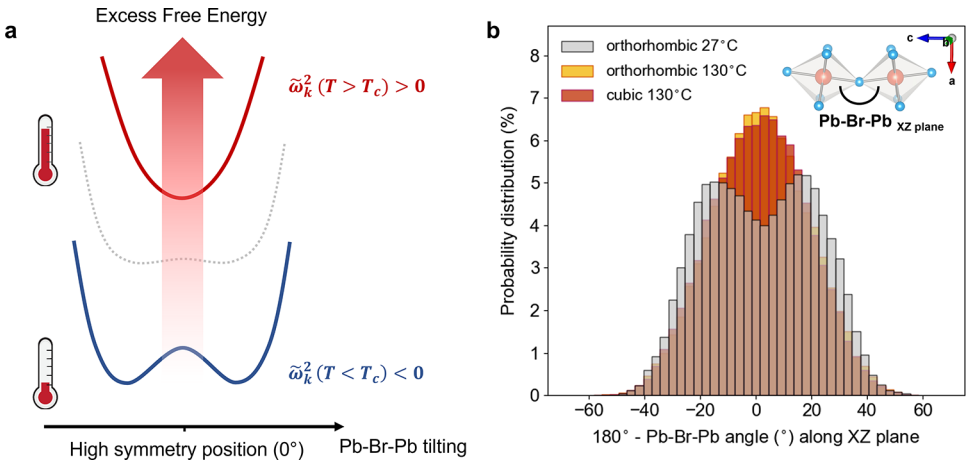

Figure 3. Theoretical predictions of the MD simulations. (a) Schematic of the excess free energy evolution with the temperature along the soft phonon coordinate of the Pb−Br−Pb octahedral tilting. The renormalized frequency of the soft phonon mode $\tilde{\omega}_k$ is temperature-dependent due to its strong anharmonicity.[36] Upon temperature increase, from bottom to top, the free energy landscape along this mode changes, causing a displacive phase transition at the critical temperature T_c. (b) Probability distribution (%) of the Pb−Br−Pb angle as a function of the angle distortion: 27 °C (orthorhombic starting geometry, gray), 130 °C (orthorhombic starting geometry, orange), and 130 °C (cubic starting geometry, red). The Pb−Br−Pb angle is projected along the XZ plane, locally describing the octahedral tilting of the Pb−Br inorganic framework. The *x*-axis reports the difference between 180° and the Pb−Br−Pb angle projection along the XZ plane in order to center the distribution at 0°, corresponding to the ideal cubic geometry. Upon temperature increase, the Pb−Br−Pb angle probability distribution is modified, changing from bimodal to monomodal across the displacive phase transition. Inset: graphical representation of the Pb−Br−Pb angle in the plane defined by the *a* and *c* crystallographic axes (XZ plane).

Therefore, our correlative approach identifies the inorganic framework flexibility as the primary feature ruling T-induced structural changes in this perovskite system, unpacking the lattice distortions that were time-averaged in previous investigations,[23,28] thanks to the agreement between experiment and theory both in the long- and short-ranges.

Sublattice disorder in the metal halide framework was observed in organic lead and tin halide perovskites.[51] The PDF structural refinements obtained from the Fourier transform of X-ray powder diffraction showed significant internal distortions of the BX_6 octahedra (with B = Pb^{2+}, Sn^{2+} and X = Cl^-, Br^-) at short interatomic distances. The presence of time-averaged orthorhombic twin domains in the high temperature phases of inorganic lead halide perovskites NCs was identified employing Debye scattering equation analysis in a X-ray total scattering study.[23] In single crystals, thermal local fluctuations of the Pb−Br framework were experimentally shown for $CsPbBr_3$ and $MAPbBr_3$ in their highest temperature phase.[22] A zero-frequency Raman peak was observed, which is normally absent in purely harmonic systems, pointing to the presence of strong anharmonicity in the lead halide framework. Similar conclusions were proposed for $MAPbI_3$ single crystals using the HERIX technique[20] and in both organic and inorganic lead iodide perovskites based on *ab initio* MD simulations.[52] In light of these findings, and based on our correlative structural characterization, we argue that the description of the system's phase diagram in terms of symmetry increasing phases upon temperature rise is too simplistic. Indeed, properties such as the unusual optical band gap increase of lead halide perovskites with the temperature, which were attributed to octahedral tilting[37,53,54] in the lattice framework, can be accurately described only accounting for an increased structural disorder.[55] As such, the description of the crystal structure through its average symmetry is misleading as it leads to incorrect evaluations of crucial physical properties of the system.

Here, we rationalize our results considering the phonon anharmonicity of the inorganic perovskite framework. Phase transitions can be described by the phenomenological Landau−Ginzburg theory, which defines the temperature dependence of the free energy as a power series in an order parameter.[56] An effective microscopic description, known as soft-mode model, was proposed from neutron diffraction studies[57] for the interpretation of structural phase transitions in oxide perovskites, which are strongly anharmonic systems. In this picture, at least one phonon frequency is substantially affected by temperature changes due to anharmonic effects. This "soft" phonon mode represents the order parameter of the phase transition. Following the renormalized phonon theory, the intrinsic dependence of the soft phonon frequency from the temperature can be espressed as[58]

$$\tilde{\omega}_{\boldsymbol{k}}^2 = \omega_{\boldsymbol{k}}^2 + \alpha \cdot T$$

where $\tilde{\omega}_{\boldsymbol{k}}$ and $\omega_{\boldsymbol{k}}$ are the renormalized and negative harmonic phonon frequencies of the soft mode with wave vector $\boldsymbol{k}$, respectively, and α is a positive factor including the anharmonicity constants of the system. $\tilde{\omega}_{\boldsymbol{k}}^2$ determines the sign of the restoring force of the system against a deformation along the soft mode coordinate. As schematically reported in Figure 3a, if $\tilde{\omega}_{\boldsymbol{k}}^2 < 0$, the free energy surface has a double-well shape with a negative curvature at the high symmetry position, and the system is stabilized by a structural distortion along the soft mode. This applies to $CsPbBr_3$, which is in the orthorhombic phase at room temperature.

In Figure 3b, the statistical distribution of the Pb−Br−Pb angle predicted by the MD simulation at 27 °C (orthorhombic starting geometry) is shown in gray. The tilting is reported as the difference between 180° and the Pb−Br−Pb angle projected along the XZ plane, such that any angular distortion with respect to the ideal cubic structure implies a deviation from the 0° value. We note that the distribution is characterized by a wide bimodal shape of the Pb−Br−Pb

https://doi.org/10.1021/acs.jpclett.2c00281
J. Phys. Chem. Lett. 2022, 13, 3382−3391

angle peaked at symmetric positions of ±16°. This result is consistent with the room temperature XRD $I(Q)$ profiles reported in Figures 2c,d, characterized by the superlattice peaks arising from the periodic tilting of the $PbBr_6$ octahedra in the system. The fit of the distribution with two identically symmetric Gaussian curves yields a standard deviation of 12° (details are reported in the SI, Figure S11).

As α is positive, a temperature increase changes the renormalized phonon frequency $\tilde{\omega}_k^2$ first to zero and then to positive values, stabilizing the cubic configuration of the system since a restoring force acts on the nuclei when they are displaced from the high symmetry position.[36] Correspondingly, the minimum of the excess free energy curve is displaced as depicted in Figure 3a. This process is thus defined "displacive" phase transition, and it is driven by T-dependent anharmonic effects. In Figure 3b, our MD simulations at 130 °C (orthorhombic and cubic initial configurations, in orange and red, respectively) show the impact of the excess free energy modification on the statistical distribution of the octahedral tilting. In fact, upon temperature increase from 27 to 130 °C the Pb−Br−Pb angle distribution drastically changes, with the high temperature curves characterized by a broad monomodal distribution centered at the high symmetry position (0°) with a standard deviation of 18°. Thus, even at 130 °C, the statistical weight of strongly distorted configurations remains relevant, with extreme absolute values up to 40−60°, which are similar to those of the orthorhombic structure at 27 °C. As such, the temperature increase mainly affects the center of the distribution, i.e., the distortions of the Pb−Br−Pb bond in proximity of the ideal cubic geometry, in agreement with the predictions of a displacive phase transition. Correspondingly, the superlattice peaks in the high temperature XRD $I(Q)$ profiles of Figure 2c,d disappear due to the loss of long-range periodicity associated with the orthorhombic tilting (Figure 1c), caused by thermal fluctuations driven by anharmonic effects.

The soft-mode model provides a microscopic description of the changes occurring in the system across the phase transition, solving the ambiguities about the presence of structural disorder in the high temperature phase of $CsPbBr_3$.[20,22,23] The soft phonon frequency undergoes a continuous change with temperature due to the phonon anharmonicity and so does the shape of the excess free energy curve. Upon temperature increase, a discontinuity in $\tilde{\omega}_k$ occurs at the phase transition temperature, defined as the temperature at which $\tilde{\omega}_k^2$ changes in sign, stabilizing the average high symmetry position even though large structural distortions remain thermally accessible. At the critical temperature, other physical properties also undergo a discontinuity, such as the linear thermal expansion coefficient[59] or the ultrasonic velocity[34] for the $CsPbBr_3$ system.

Long-range structural techniques probe the average lattice geometry of the system, which in the highest temperature phase is centered in the cubic symmetry positions. However, the thermal dynamics determine strong local distortions of the lattice, which can be observed only exploiting short-range structural characterization methods such as the XANES spectroscopy used here. Since the XANES signal originates from the statistical average of all local configurations of the probed sites, at high temperature and for this dynamic system, this observable cannot be reproduced with a unique structure having averaged lattice parameters as those obtained in PDF refinements. To our knowledge, the effect of thermal disorder on the XANES spectra was successfully reproduced only for systems in which the harmonic approximation of the phonon modes is appropriate.[47,60] Therefore, here we demonstrate that the impact of thermal dynamics on the XANES spectra can be effectively described also for largely anharmonic systems such as lead halide perovskites when *ab initio* MD simulations—to determine the dynamically fluctuating structures—are combined with calculations accounting for core hole final state effects to retrieve an accurate XANES line shape. Previous works characterized different sources of disorder at the local scale in the perovskite systems using PDF methods but mostly relied on *a posteriori* strategies in which a single time-averaged structure was considered, proposing only qualitative arguments to reconcile their inconsistency with longer range results, which agree with high symmetry structures.[23,51]

Combining both short- and long-range experimental methods with simulations, we are thus able to provide a complete description of the thermal structural changes in $CsPbBr_3$ perovskites that is rationalized through the soft-mode model. Since this theoretical framework relies on the lattice flexibility and phonon anharmonicity of the system, we argue that the soft-mode model carries a more general validity in describing displacive thermal phase transitions in perovskites, be it oxide or lead halide and, for the latter, either inorganic or organic. Indeed, a recent T-dependent neutron scattering study reported the presence of a soft mode in $MAPbBr_3$ single crystals,[61] with the results being likewise interpreted in terms of displacive thermal phase transitions driven by the $PbBr_6$ octahedral tilting. Due to the common Pb−Br framework of organic and inorganic lead bromide perovskites, we can ascribe the consecutive phase transitions in $CsPbBr_3$ to T-dependent anharmonic effects of the $PbBr_6$ tilting mode, with the soft mode representing the order parameter of the inorganic perovskite system. The proposed scenario is also consistent with recent observations reported in ref 54.

Our analysis of the lattice thermal dynamics also helps in clarifying and quantifying the effects underlying the characteristic band gap blue shift of lead halide perovskites with the temperature rise. In the literature, it is established that both lattice expansion and octahedral tilting affect the band gap energy.[53] These structural modifications widen the band gap by decreasing the lead-halogen orbital overlap, which leads to a shift of the valence band maximum toward lower energies due to its antibonding character. Having a stronger nonbonding character, the conduction band minimum is less affected by these structural changes, resulting in a net blue shift of the band gap, which in the case of $CsPbBr_3$ was observed to increase about 20 meV by warming up the system from room temperature up to 150 °C.[37] Over this temperature range, the lattice expansion leads to a band gap energy increase of ∼10 meV,[37] meaning that an increased octahedral tilting should account for the residual contribution. This, however, contrasts with the predictions of a symmetry increase of the average structure. Previous DFT calculations explained the blue shift of the band gap by comparing the effect of the octahedral tilting with respect to an ideal cubic structure at 0 K, leading to changes of hundreds of meV.[37,54,55] Even though these simulations show a correlation between structural deformations and band gap energies, they do not reproduce the physical process occurring upon thermal heating of the system. Our results clarify the reason why the band gap changes due to thermal structural dynamics are much smaller for temperatures above 300 K. By comparing room temperature and high

https://doi.org/10.1021/acs.jpclett.2c00281
J. Phys. Chem. Lett. 2022, 13, 3382−3391

temperature MD simulations, we show that thermal fluctuations lead to a reduction of the local symmetry without a significant change of the maximum amplitude of the Pb−Br−Pb tilting (Figure 3b). Since the blue shift of the band gap is related to the magnitude of the octahdral tilting, this finding explains the small influcence of the pronounced local disorder on the optical band gap of the system, with T-induced energy changes below the accuracy of DFT methods.

In conclusion, in this work we provide a consistent microscopic description of the thermal dynamics of $CsPbBr_3$ combining short- and long-range structural sensitive techniques with *ab initio* MD simulations. Based on the agreement between theory and experiments, we harness our first-principles results to precisely quantify the thermal fluctuations of the system, retrieving unprecedented details on the T-dependent structural changes and their effects on the system's properties.

The atomic-level picture emerging from the correlative characterization of $CsPbBr_3$ is very different from the light-driven structural changes observed in $CsPbBr_3$ NCs with time-resolved XANES:[26] upon above band gap excitation, large polarons are formed due to the electron−phonon coupling between the photocarriers and the polar inorganic lattice. The crystal distortion involves the activation of one specific longitudinal-optical phonon mode, implying well-defined nuclear displacements of the Pb−Br sublattice, which can be retrieved with atomic-scale precision by the analysis of the transient spectra. Instead, the high temperature configuration of the system is dynamically distorted and cannot be reduced, at the local scale, to an average ordered structure, thereby questioning the classical picture of a low-to-high symmetry phase transition.

These results clarify the underlying mechanisms of the lattice response under functional activation and offers strategies to control the perovskite nuclear degrees of freedom with different external stimuli. Understanding the thermal processes acting at the atomic level represents the first step toward a rational design of perovskite-based devices with improved stability.

■ ASSOCIATED CONTENT

Supporting Information

The Supporting Information is available free of charge at https://pubs.acs.org/doi/10.1021/acs.jpclett.2c00281.

(1) Samples and characterization, (2) $CsPbBr_3$ model crystal structures and XRD, (3) T-dependent XRD and XANES data analysis, (4) MD computational methods, (5) XANES computational methods, (6) volume expansion contribution to T-dependent XANES changes, (7) time evolution of Pb−Br−Pb angle distribution in MD simulations, (8) thermal displacements of Cs, Pb, and Br sites in MD simulations (PDF)

■ AUTHOR INFORMATION

Corresponding Authors

Giulia F. Mancini − *Laboratory for Ultrafast X-ray and Electron Microscopy (LUXEM), Department of Physics, University of Pavia, I-27100 Pavia, Italy;* orcid.org/0000-0002-7752-2822; Email: giuliafulvia.mancini@unipv.it

Majed Chergui − *Laboratory of Ultrafast Spectroscopy (LSU) and Lausanne Centre for Ultrafast Science (LACUS), École Polytechnique Fédérale de Lausanne, CH-1015 Lausanne, Switzerland;* orcid.org/0000-0002-4856-226X; Email: majed.chergui@epfl.ch

Authors

Oliviero Cannelli − *Laboratory of Ultrafast Spectroscopy (LSU) and Lausanne Centre for Ultrafast Science (LACUS), École Polytechnique Fédérale de Lausanne, CH-1015 Lausanne, Switzerland;* orcid.org/0000-0002-1844-4799

Julia Wiktor − *Department of Physics, Chalmers University of Technology, SE-412 96 Gothenburg, Sweden;* orcid.org/0000-0003-3395-1104

Nicola Colonna − *Laboratory for Neutron Scattering and Imaging, Paul Scherrer Institute, CH-5232 Villigen-PSI, Switzerland; National Centre for Computational Design and Discovery of Novel Materials (MARVEL), École Polytechnique Fédérale de Lausanne, CH-1015 Lausanne, Switzerland;* orcid.org/0000-0002-6106-6316

Ludmila Leroy − *Laboratory of Ultrafast Spectroscopy (LSU) and Lausanne Centre for Ultrafast Science (LACUS), École Polytechnique Fédérale de Lausanne, CH-1015 Lausanne, Switzerland; LabCri, Departamento de Física, Universidade Federal de Minas Gerais, 31270-901 Belo Horizonte, Brazil;* orcid.org/0000-0002-4272-0298

Michele Puppin − *Laboratory of Ultrafast Spectroscopy (LSU) and Lausanne Centre for Ultrafast Science (LACUS), École Polytechnique Fédérale de Lausanne, CH-1015 Lausanne, Switzerland;* orcid.org/0000-0002-1328-7165

Camila Bacellar − *Paul Scherrer Institute (PSI), CH-5232 Villigen, Switzerland;* orcid.org/0000-0003-2166-241X

Ilia Sadykov − *Paul Scherrer Institute (PSI), CH-5232 Villigen, Switzerland;* orcid.org/0000-0003-1549-4771

Franziska Krieg − *Institute of Inorganic Chemistry, Department of Chemistry and Applied Biosciences, ETH Zürich, CH-8093 Zürich, Switzerland; Laboratory for Thin Films and Photovoltaics, Empa-Swiss Federal Laboratories for Materials Science and Technology, CH-8600 Dübendorf, Switzerland;* orcid.org/0000-0002-0370-1318

Grigory Smolentsev − *Paul Scherrer Institute (PSI), CH-5232 Villigen, Switzerland;* orcid.org/0000-0001-7348-7276

Maksym V. Kovalenko − *Institute of Inorganic Chemistry, Department of Chemistry and Applied Biosciences, ETH Zürich, CH-8093 Zürich, Switzerland; Laboratory for Thin Films and Photovoltaics, Empa-Swiss Federal Laboratories for Materials Science and Technology, CH-8600 Dübendorf, Switzerland;* orcid.org/0000-0002-6396-8938

Alfredo Pasquarello − *Chaire de Simulation à l'Echelle Atomique (CSEA), École Polytechnique Fédérale de Lausanne (EPFL), CH-1015 Lausanne, Switzerland;* orcid.org/0000-0002-9142-2799

Complete contact information is available at: https://pubs.acs.org/10.1021/acs.jpclett.2c00281

Notes

The authors declare no competing financial interest.

Processed data showed in this manuscript are available in the Supporting Information. Raw data are available in the following repository: 10.5281/zenodo.4928983.

■ ACKNOWLEDGMENTS

This work was supported by the European Union's Horizon 2020 research and innovation program, through the grant agreement no. 851154 (ULTRAIMAGE) and no. 695197 755

(DYNAMOX). G.F.M. acknowledges funding from Fondazione Cariplo (NanoFast 2020.2544). J.W. acknowledges funding from the Swedish Research Council (2019-03993) and the Chalmers Gender Initiative for Excellence (Genie). The computations were performed on resources provided by the Swedish National Infrastructure for Computing (SNIC) at NSC, C3SE, and PDC. N.C. acknowledges the support of by the SwissNSF NCCR-MARVEL. M.K. acknowledges funding by the European Union's Horizon 2020 program, through a FET Open research and innovation action under the grant agreement no. 899141 (PoLLoC). We thank Balázs Őrley for the graphical rendering of Figure 1a.

REFERENCES

(1) Berhe, T. A.; Su, W.-N.; Chen, C.-H.; Pan, C.-J.; Cheng, J.-H.; Chen, H.-M.; Tsai, M.-C.; Chen, L.-Y.; Aregahegn Dubale, A.; Hwang, B.-J. Organometal Halide Perovskite Solar Cells: Degradation and Stability. *Energy Environ. Sci.* **2016**, *9* (2), 323−356.

(2) Correa-Baena, J.-P.; Saliba, M.; Buonassisi, T.; Grätzel, M.; Abate, A.; Tress, W.; Hagfeldt, A. Promises and Challenges of Perovskite Solar Cells. *Science* **2017**, *358* (6364), 739−744.

(3) Nayak, P. K.; Mahesh, S.; Snaith, H. J.; Cahen, D. Photovoltaic Solar Cell Technologies: Analysing the State of the Art. *Nat. Rev. Mater.* **2019**, *4* (4), 269−285.

(4) Liu, X.-K.; Xu, W.; Bai, S.; Jin, Y.; Wang, J.; Friend, R. H.; Gao, F. Metal Halide Perovskites for Light-Emitting Diodes. *Nat. Mater.* **2021**, *20*, 10−21.

(5) Leijtens, T.; Eperon, G. E.; Pathak, S.; Abate, A.; Lee, M. M.; Snaith, H. J. Overcoming Ultraviolet Light Instability of Sensitized TiO_2 with Meso-Superstructured Organometal Tri-Halide Perovskite Solar Cells. *Nat. Commun.* **2013**, *4* (1), 2885.

(6) Wang, D.; Wright, M.; Elumalai, N. K.; Uddin, A. Stability of Perovskite Solar Cells. *Sol. Energy Mater. Sol. Cells* **2016**, *147*, 255−275.

(7) Slavney, A. H.; Smaha, R. W.; Smith, I. C.; Jaffe, A.; Umeyama, D.; Karunadasa, H. I. Chemical Approaches to Addressing the Instability and Toxicity of Lead−Halide Perovskite Absorbers. *Inorg. Chem.* **2017**, *56* (1), 46−55.

(8) Nedelcu, G.; Protesescu, L.; Yakunin, S.; Bodnarchuk, M. I.; Grotevent, M. J.; Kovalenko, M. V. Fast Anion-Exchange in Highly Luminescent Nanocrystals of Cesium Lead Halide Perovskites ($CsPbX_3$, X = Cl, Br, I). *Nano Lett.* **2015**, *15* (8), 5635−5640.

(9) Bischak, C. G.; Hetherington, C. L.; Wu, H.; Aloni, S.; Ogletree, D. F.; Limmer, D. T.; Ginsberg, N. S. Origin of Reversible Photoinduced Phase Separation in Hybrid Perovskites. *Nano Lett.* **2017**, *17* (2), 1028−1033.

(10) Stranks, S. D.; Snaith, H. J. Metal-Halide Perovskites for Photovoltaic and Light-Emitting Devices. *Nat. Nanotechnol.* **2015**, *10* (5), 391−402.

(11) Smith, I. C.; Hoke, E. T.; Solis-Ibarra, D.; McGehee, M. D.; Karunadasa, H. I. A Layered Hybrid Perovskite Solar-Cell Absorber with Enhanced Moisture Stability. *Angew. Chem., Int. Ed.* **2014**, *126* (42), 11414−11417.

(12) Hintermayr, V. A.; Lampe, C.; Löw, M.; Roemer, J.; Vanderlinden, W.; Gramlich, M.; Böhm, A. X.; Sattler, C.; Nickel, B.; Lohmüller, T.; Urban, A. S. Polymer Nanoreactors Shield Perovskite Nanocrystals from Degradation. *Nano Lett.* **2019**, *19* (8), 4928−4933.

(13) Pisoni, A.; Jaćimović, J.; Barišić, O. S.; Spina, M.; Gaál, R.; Forró, L.; Horváth, E. Ultra-Low Thermal Conductivity in Organic−Inorganic Hybrid Perovskite $CH_3NH_3PbI_3$. *J. Phys. Chem. Lett.* **2014**, *5* (14), 2488−2492.

(14) Mettan, X.; Pisoni, R.; Matus, P.; Pisoni, A.; Jaćimović, J.; Náfrádi, B.; Spina, M.; Pavuna, D.; Forró, L.; Horváth, E. Tuning of the Thermoelectric Figure of Merit of $CH_3NH_3MI_3$ (M = Pb,Sn) Photovoltaic Perovskites. *J. Phys. Chem. C* **2015**, *119* (21), 11506−11510.

(15) Lee, W.; Li, H.; Wong, A. B.; Zhang, D.; Lai, M.; Yu, Y.; Kong, Q.; Lin, E.; Urban, J. J.; Grossman, J. C.; Yang, P. Ultralow Thermal Conductivity in All-Inorganic Halide Perovskites. *Proc. Natl. Acad. Sci. U.S.A.* **2017**, *114* (33), 8693−8697.

(16) Akkerman, Q. A.; Rainò, G.; Kovalenko, M. V.; Manna, L. Genesis, Challenges and Opportunities for Colloidal Lead Halide Perovskite Nanocrystals. *Nat. Mater.* **2018**, *17* (5), 394−405.

(17) Grancini, G.; Nazeeruddin, M. K. Dimensional Tailoring of Hybrid Perovskites for Photovoltaics. *Nat. Rev. Mater.* **2019**, *4* (1), 4−22.

(18) Miyata, K.; Meggiolaro, D.; Trinh, M. T.; Joshi, P. P.; Mosconi, E.; Jones, S. C.; Angelis, F. D.; Zhu, X.-Y. Large Polarons in Lead Halide Perovskites. *Sci. Adv.* **2017**, *3* (8), No. e1701217.

(19) Miyata, K.; Atallah, T. L.; Zhu, X.-Y. Lead Halide Perovskites: Crystal-Liquid Duality, Phonon Glass Electron Crystals, and Large Polaron Formation. *Sci. Adv.* **2017**, *3* (10), No. e1701469.

(20) Beecher, A. N.; Semonin, O. E.; Skelton, J. M.; Frost, J. M.; Terban, M. W.; Zhai, H.; Alatas, A.; Owen, J. S.; Walsh, A.; Billinge, S. J. L. Direct Observation of Dynamic Symmetry Breaking above Room Temperature in Methylammonium Lead Iodide Perovskite. *ACS Energy Lett.* **2016**, *1* (4), 880−887.

(21) Cottingham, P.; Brutchey, R. L. Depressed Phase Transitions and Thermally Persistent Local Distortions in $CsPbBr_3$ Quantum Dots. *Chem. Mater.* **2018**, *30* (19), 6711−6716.

(22) Yaffe, O.; Guo, Y.; Tan, L. Z.; Egger, D. A.; Hull, T.; Stoumpos, C. C.; Zheng, F.; Heinz, T. F.; Kronik, L.; Kanatzidis, M. G.; Owen, J. S.; Rappe, A. M.; Pimenta, M. A.; Brus, L. E. Local Polar Fluctuations in Lead Halide Perovskite Crystals. *Phys. Rev. Lett.* **2017**, *118* (13), 136001.

(23) Bertolotti, F.; Protesescu, L.; Kovalenko, M. V.; Yakunin, S.; Cervellino, A.; Billinge, S. J. L.; Terban, M. W.; Pedersen, J. S.; Masciocchi, N.; Guagliardi, A. Coherent Nanotwins and Dynamic Disorder in Cesium Lead Halide Perovskite Nanocrystals. *ACS Nano* **2017**, *11* (4), 3819−3831.

(24) Gu, H.-Y.; Yin, W.-J.; Gong, X.-G. Significant Phonon Anharmonicity Drives Phase Transitions in $CsPbI_3$. *Appl. Phys. Lett.* **2021**, *119* (19), 191101.

(25) Lai, M.; Obliger, A.; Lu, D.; Kley, C. S.; Bischak, C. G.; Kong, Q.; Lei, T.; Dou, L.; Ginsberg, N. S.; Limmer, D. T.; Yang, P. Intrinsic Anion Diffusivity in Lead Halide Perovskites Is Facilitated by a Soft Lattice. *Proc. Natl. Acad. Sci. U. S. A.* **2018**, *115* (47), 11929−11934.

(26) Cannelli, O.; Colonna, N.; Puppin, M.; Rossi, T. C.; Kinschel, D.; Leroy, L. M. D.; Löffler, J.; Budarz, J. M.; March, A. M.; Doumy, G.; Al Haddad, A.; Tu, M.-F.; Kumagai, Y.; Walko, D.; Smolentsev, G.; Krieg, F.; Boehme, S. C.; Kovalenko, M. V.; Chergui, M.; Mancini, G. F. Quantifying Photoinduced Polaronic Distortions in Inorganic Lead Halide Perovskite Nanocrystals. *J. Am. Chem. Soc.* **2021**, *143* (24), 9048−9059.

(27) Hirotsu, S.; Harada, J.; Iizumi, M.; Gesi, K. Structural Phase Transitions in $CsPbBr_3$. *J. Phys. Soc. Jpn.* **1974**, *37* (5), 1393−1398.

(28) Stoumpos, C. C.; Malliakas, C. D.; Peters, J. A.; Liu, Z.; Sebastian, M.; Im, J.; Chasapis, T. C.; Wibowo, A. C.; Chung, D. Y.; Freeman, A. J.; Wessels, B. W.; Kanatzidis, M. G. Crystal Growth of the Perovskite Semiconductor $CsPbBr_3$: A New Material for High-Energy Radiation Detection. *Cryst. Growth Des.* **2013**, *13* (7), 2722−2727.

(29) Møller, C. K. The Structure of Perovskite-like Caesium Plumbo Trihalides. *Mater. Fys. Medd Danske Vidensk Selsk.* 1959, *32* (2).

(30) Vanacore, G. M.; Hu, J.; Liang, W.; Bietti, S.; Sanguinetti, S.; Zewail, A. H. Diffraction of Quantum Dots Reveals Nanoscale Ultrafast Energy Localization. *Nano Lett.* **2014**, *14* (11), 6148−6154.

(31) Krieg, F.; Ochsenbein, S. T.; Yakunin, S.; ten Brinck, S.; Aellen, P.; Süess, A.; Clerc, B.; Guggisberg, D.; Nazarenko, O.; Shynkarenko, Y.; Kumar, S.; Shih, C.-J.; Infante, I.; Kovalenko, M. V. Colloidal $CsPbX_3$ (X = Cl, Br, I) Nanocrystals 2.0: Zwitterionic Capping Ligands for Improved Durability and Stability. *ACS Energy Lett.* **2018**, *3* (3), 641−646.

(32) Guzelturk, B.; Utterback, J. K.; Coropceanu, I.; Kamysbayev, V.; Janke, E. M.; Zajac, M.; Yazdani, N.; Cotts, B. L.; Park, S.; Sood,

https://doi.org/10.1021/acs.jpclett.2c00281
J. Phys. Chem. Lett. 2022, 13, 3382−3391

A.; Lin, M.-F.; Reid, A. H.; Kozina, M. E.; Shen, X.; Weathersby, S. P.; Wood, V.; Salleo, A.; Wang, X.; Talapin, D. V.; Ginsberg, N. S.; Lindenberg, A. M. Nonequilibrium Thermodynamics of Colloidal Gold Nanocrystals Monitored by Ultrafast Electron Diffraction and Optical Scattering Microscopy. *ACS Nano* **2020**, *14* (4), 4792−4804.
(33) Mancini, G. F.; Pennacchio, F.; Latychevskaia, T.; Reguera, J.; Stellacci, F.; Carbone, F. Local Photo-Mechanical Stiffness Revealed in Gold Nanoparticles Supracrystals by Ultrafast Small-Angle Electron Diffraction. *Structural Dynamics* **2019**, *6* (2), 024304.
(34) Hirotsu, S.; Suzuki, T.; Sawada, S. Ultrasonic Velocity around the Successive Phase Transition Points of $CsPbBr_3$. *J. Phys. Soc. Jpn.* **1977**, *43* (2), 575−582.
(35) Bechtel, J. S.; Thomas, J. C.; Van der Ven, A. Finite-Temperature Simulation of Anharmonicity and Octahedral Tilting Transitions in Halide Perovskites. *Phys. Rev. Mater.* **2019**, *3* (11), 113605.
(36) Dove, M. T. Theory of Displacive Phase Transitions in Minerals. *Am. Mineral.* **1997**, *82* (3−4), 213−244.
(37) Mannino, G.; Deretzis, I.; Smecca, E.; La Magna, A.; Alberti, A.; Ceratti, D.; Cahen, D. Temperature-Dependent Optical Band Gap in $CsPbBr_3$, $MAPbBr_3$, and $FAPbBr_3$ Single Crystals. *J. Phys. Chem. Lett.* **2020**, *11* (7), 2490−2496.
(38) Momma, K.; Izumi, F. VESTA 3 for Three-Dimensional Visualization of Crystal, Volumetric and Morphology Data. *J. Appl. Crystallogr.* **2011**, *44* (6), 1272−1276.
(39) VandeVondele, J.; Krack, M.; Mohamed, F.; Parrinello, M.; Chassaing, T.; Hutter, J. Quickstep: Fast and Accurate Density Functional Calculations Using a Mixed Gaussian and Plane Waves Approach. *Comput. Phys. Commun.* **2005**, *167* (2), 103−128.
(40) Perdew, J. P.; Burke, K.; Ernzerhof, M. Generalized Gradient Approximation Made Simple. *Phys. Rev. Lett.* **1996**, *77* (18), 3865−3868.
(41) Giannozzi, P.; Baroni, S.; Bonini, N.; Calandra, M.; Car, R.; Cavazzoni, C.; Ceresoli, D.; Chiarotti, G. L.; Cococcioni, M.; Dabo, I.; Dal Corso, A.; Gironcoli, S. de; Fabris, S.; Fratesi, G.; Gebauer, R.; Gerstmann, U.; Gougoussis, C.; Kokalj, A.; Lazzeri, M.; Martin-Samos, L.; Marzari, N.; Mauri, F.; Mazzarello, R.; Paolini, S.; Pasquarello, A.; Paulatto, L.; Sbraccia, C.; Scandolo, S.; Sclauzero, G.; Seitsonen, A. P.; Smogunov, A.; Umari, P.; Wentzcovitch, R. M. QUANTUM ESPRESSO: A Modular and Open-Source Software Project for Quantum Simulations of Materials. *J. Phys.: Condens. Matter* **2009**, *21* (39), 395502.
(42) Giannozzi, P.; Andreussi, O.; Brumme, T.; Bunau, O.; Nardelli, M. B.; Calandra, M.; Car, R.; Cavazzoni, C.; Ceresoli, D.; Cococcioni, M.; Colonna, N.; Carnimeo, I.; Dal Corso, A.; Gironcoli, S. de; Delugas, P.; DiStasio, R. A.; Ferretti, A.; Floris, A.; Fratesi, G.; Fugallo, G.; Gebauer, R.; Gerstmann, U.; Giustino, F.; Gorni, T.; Jia, J.; Kawamura, M.; Ko, H.-Y.; Kokalj, A.; Küçükbenli, E.; Lazzeri, M.; Marsili, M.; Marzari, N.; Mauri, F.; Nguyen, N. L.; Nguyen, H.-V.; Otero-de-la-Roza, A.; Paulatto, L.; Poncé, S.; Rocca, D.; Sabatini, R.; Santra, B.; Schlipf, M.; Seitsonen, A. P.; Smogunov, A.; Timrov, I.; Thonhauser, T.; Umari, P.; Vast, N.; Wu, X.; Baroni, S. Advanced Capabilities for Materials Modelling with Quantum ESPRESSO. *J. Phys.: Condens. Matter* **2017**, *29* (46), 465901.
(43) Dal Corso, A. Pseudopotentials Periodic Table: From H to Pu. *Comput. Mater. Sci.* **2014**, *95*, 337−350.
(44) Taillefumier, M.; Cabaret, D.; Flank, A.-M.; Mauri, F. X-Ray Absorption near-Edge Structure Calculations with the Pseudopotentials: Application to the *K* Edge in Diamond and α-Quartz. *Phys. Rev. B* **2002**, *66* (19), 195107.
(45) Gougoussis, C.; Calandra, M.; Seitsonen, A. P.; Mauri, F. First-Principles Calculations of X-Ray Absorption in a Scheme Based on Ultrasoft Pseudopotentials: From α-Quartz to High-T_c Compounds. *Phys. Rev. B* **2009**, *80* (7), 075102.
(46) Prendergast, D.; Galli, G. X-Ray Absorption Spectra of Water from First Principles Calculations. *Phys. Rev. Lett.* **2006**, *96* (21), 215502.
(47) Nemausat, R.; Gervais, C.; Brouder, C.; Trcera, N.; Bordage, A.; Coelho-Diogo, C.; Florian, P.; Rakhmatullin, A.; Errea, I.; Paulatto, L.; Lazzeri, M.; Cabaret, D. Temperature Dependence of X-Ray Absorption and Nuclear Magnetic Resonance Spectra: Probing Quantum Vibrations of Light Elements in Oxides. *Phys. Chem. Chem. Phys.* **2017**, *19* (8), 6246−6256.
(48) Rehr, J. J.; Albers, R. C. Theoretical Approaches to X-Ray Absorption Fine Structure. *Rev. Mod. Phys.* **2000**, *72* (3), 621−654.
(49) Teo, B. K. *EXAFS: Basic Principles and Data Analysis*; Springer Science & Business Media, 2012.
(50) Glazer, A. M. Simple Ways of Determining Perovskite Structures. *Acta Crystallogr., Sect. A: Found. Crystallogr.* **1975**, *31* (6), 756−762.
(51) Worhatch, R. J.; Kim, H.; Swainson, I. P.; Yonkeu, A. L.; Billinge, S. J. L. Study of Local Structure in Selected Organic−Inorganic Perovskites in the $Pm\bar{3}m$ Phase. *Chem. Mater.* **2008**, *20* (4), 1272−1277.
(52) Carignano, M. A.; Aravindh, S. A.; Roqan, I. S.; Even, J.; Katan, C. Critical Fluctuations and Anharmonicity in Lead Iodide Perovskites from Molecular Dynamics Supercell Simulations. *J. Phys. Chem. C* **2017**, *121* (38), 20729−20738.
(53) Prasanna, R.; Gold-Parker, A.; Leijtens, T.; Conings, B.; Babayigit, A.; Boyen, H.-G.; Toney, M. F.; McGehee, M. D. Band Gap Tuning via Lattice Contraction and Octahedral Tilting in Perovskite Materials for Photovoltaics. *J. Am. Chem. Soc.* **2017**, *139* (32), 11117−11124.
(54) Lanigan-Atkins, T.; He, X.; Krogstad, M. J.; Pajerowski, D. M.; Abernathy, D. L.; Xu, G. N. M. N.; Xu, Z.; Chung, D.-Y.; Kanatzidis, M. G.; Rosenkranz, S.; Osborn, R.; Delaire, O. Two-Dimensional Overdamped Fluctuations of the Soft Perovskite Lattice in $CsPbBr_3$. *Nat. Mater.* **2021**, *20* (7), 977−983.
(55) Wiktor, J.; Rothlisberger, U.; Pasquarello, A. Predictive Determination of Band Gaps of Inorganic Halide Perovskites. *J. Phys. Chem. Lett.* **2017**, *8* (22), 5507−5512.
(56) Bruce, A. D.; Cowley, R. A. *Structural Phase Transitions*; Monographs on physics; Taylor & Francis: London, 1981.
(57) Shirane, G. Neutron Scattering Studies of Structural Phase Transitions at Brookhaven. *Rev. Mod. Phys.* **1974**, *46* (3), 437−449.
(58) Dove, M. T. *Introduction to Lattice Dynamics*; Cambridge University Press: Cambridge, 1993.
(59) Rodová, M.; Brožek, J.; Knížek, K.; Nitsch, K. Phase Transitions in Ternary Caesium Lead Bromide. *J. Therm. Anal. Calorim.* **2003**, *71* (2), 667−673.
(60) Nemausat, R.; Cabaret, D.; Gervais, C.; Brouder, C.; Trcera, N.; Bordage, A.; Errea, I.; Mauri, F. Phonon Effects on X-Ray Absorption and Nuclear Magnetic Resonance Spectroscopies. *Phys. Rev. B* **2015**, *92* (14), 144310.
(61) Swainson, I. P.; Stock, C.; Parker, S. F.; Van Eijck, L.; Russina, M.; Taylor, J. W. From Soft Harmonic Phonons to Fast Relaxational Dynamics in $CH_3NH_3PbBr_3$. *Phys. Rev. B* **2015**, *92* (10), 100303.

https://doi.org/10.1021/acs.jpclett.2c00281
J. Phys. Chem. Lett. 2022, 13, 3382−3391